Reaction Chemistry & Engineering

ROYAL SOCIETY OF CHEMISTRY

PAPER

View Article Online
View Journal | View Issue

Cite this: *React. Chem. Eng.*, 2025, 10, 2607

The effect of hydrophilic properties of carbon-supported catalysts for the water–gas shift reaction: a kinetic study

Yapeng Zhan, [a] Yongxiang Guo,[a] Peng Wang,[abc] Riyang Shu, [a] Libin Lei,[a] Chao Wang, [a] Zhipeng Tian, *[ab] Qingbin Song*[b] and Ying Chen[a]

Carbon-supported catalysts have been widely investigated and applied in the catalytic reforming reaction and water–gas shift reaction (WGS) for hydrogen production due to their remarkable stability and superior catalytic activity. However, the effect of hydrophilic–hydrophobic properties of carbon-supported catalysts on catalytic performance remains unclear. Among the Pt-based Mn and K co-modified carbon-supported catalysts developed in this study, the catalyst modified with $KMnO_4$ exhibited the best performance in methanol steam reforming. The $KMnO_4$ treatment introduced abundant oxygen-containing functional groups and oxygen vacancies on the carbon support, significantly enhancing its hydrophilicity and water adsorption capacity. This facilitated the activation and dissociation of water molecules, which is the rate-determining step in the WGS reaction. The synergistic effect of improved hydrophilicity and increased oxygen vacancies promoted the overall reaction process, thereby enhancing the catalytic performance. Kinetic analysis of the WGS reaction was conducted between 150 °C and 250 °C, using a power-law model to fit experimental data and calculate apparent activation energies. The PtMnK/AC-Ox catalyst exhibited a significantly lower apparent activation energy of 33.1 kJ mol^{-1}, compared to 54.6 kJ mol^{-1} for the PtMnK/AC catalyst. This lower activation energy highlights the superior performance of the catalyst for the WGS reaction, particularly in promoting efficient CO conversion.

Received 12th June 2025,
Accepted 17th July 2025

DOI: 10.1039/d5re00259a

rsc.li/reaction-engineering

1. Introduction

Development of human society has led to an escalating demand for energy, making the rational development and efficient utilization of sustainable energy vital areas of research.[1] Among various types of clean energy, hydrogen distinguishes itself with high energy density and no greenhouse gas emission, presenting extensive potential for applications in various areas.[2] However, hydrogen storage and transportation involve significant safety challenges, primarily due to concerns like hydrogen embrittlement which tends to compromise transportation materials' integrity.[3,4] Methanol, with its high hydrogen content and ease of storage and transport, presents a promising alternative for hydrogen production by steam reforming (SR) or aqueous phase reforming (APR), and is a promising liquid organic hydrogen carrier.[5,6] For hydrogen production through catalytic reforming of methanol, the as-obtained gaseous products usually include CO and H_2.[7,8] In proton exchange membrane fuel cells, excessive CO concentrations can lead to poisoning of Pt electrodes, significantly impairing their performance.[9–11] The water–gas shift (WGS) reaction ($CO + H_2O \rightarrow CO_2 + H_2$) is an essential reaction for upgrading of fuel gas from biomass gasification, pyrolysis, reforming reaction, *etc.*, which plays a critical role in optimizing syngas quality.[12] One of the primary advantages of the WGS reaction is its ability to simultaneously remove CO and produce H_2, allowing the adjustment of the H_2/CO ratio in syngas. This enhances the hydrogen content of the product and mitigates the adverse effects of CO on subsequent processes by controlling the elementary steps of the WGS reaction, including CO adsorption and reaction, water dissociation, and hydrogen formation. According to previous studies, the WGS reaction rate is primarily regulated by water dissociation, which can be facilitated by highly active metals such as Pt and Cu, as well as basic sites on the catalyst support.[13,14] Traditionally, copper, zinc, and aluminum-based catalysts have been favored for the WGS reaction due to their high initial activity and cost efficiency.[12,15–18] However, their significant limitation lies in their susceptibility to catalyst deactivation, which results in a decline in catalytic

[a] *Guangdong Provincial Key Laboratory of Functional Soft Condensed Matter, School of Materials and Energy, Guangdong University of Technology, Guangzhou 510006, PR China. E-mail: tianzhipeng@gdut.edu.cn*
[b] *Macao Environmental Research Institute, Macao University of Science and Technology, Macao SAR 999078, PR China. E-mail: qbsong@must.edu.cn*
[c] *Power China Jiangxi Electric Power Construction Co., Ltd, Nanchang 331000, PR China*

performance. To address these challenges, the focus has shifted towards platinum-based catalysts, which are recognized for their excellent stability and high catalytic activity over a wide temperature range, making them promising alternatives.[19] Pt catalysts supported on CeO_2 or modified CeO_2 have shown promising WGS reaction performance, but they are still prone to metal particle sintering under high-temperature conditions, which limits their industrial applicability.[20] In response, research has increasingly turned towards carbon-supported Pt catalysts.[21] Firstly, carbon supports offer substantial flexibility in surface modification. Through surface chemical adjustments and structural optimization, the active sites on these catalysts can be effectively tuned to improve the overall catalytic performance. Despite the potential of these catalysts, Pt-based catalysts on carbon supports face a critical problem——their intrinsic WGS activity is lower than those on traditional metal oxide supports, especially when the catalyst surface is not modified. Recent studies suggest that incorporating suitable surface treatments or promoters can significantly enhance their activity.[22,23] Surface modifications, such as introducing oxygen groups or nitrogen doping, have been shown to enhance the adsorption and dissociation efficiency of water molecules, while also strengthening the electronic interactions between Pt and its support, thus improving the reaction rate. Secondly, modulating the pore structure and surface area of the carbon support increases the dispersion of Pt nanoparticles, reducing sintering at high temperatures. And the structural stability of carbon support improves the catalyst stability.[24–26] Therefore, combining surface modifications with promoters has emerged as an effective strategy to boost WGS activity in carbon supported catalysts. For example, Schweitzer *et al.* demonstrated that a 4 wt% Pt/Mo_2C catalyst showed lower activation energy and higher activity in the WGS reaction compared to other catalysts, with characterization revealing a small contact angle between Pt particles and Mo_2C, indicating excellent noble metal particle dispersion.[27]

Enhancing the hydrophilicity of carbon supports has been shown to improve methanol APR reaction performance while effectively limiting methanation, as indicated in our previous research.[28] This demonstrated that increased hydrophilicity boosts hydrogen production yield. In heterogeneous catalytic systems, adsorption and desorption of reactants and intermediates play a crucial role in affecting reactivity and gas product distribution.[29] Earlier studies have highlighted that the hydrophobic nature of carbon supports negatively impacts reforming efficiency and increases alkane selectivity. In contrast, catalysts with hydrophilic surfaces exhibit superior properties for hydrogen production, especially in APR, which reacts in a water-rich environment. The hydrophilic properties of the carbon surface contribute to the adsorption and dissociation of water more effectively, which improves the transformation of the CO intermediate and accelerates the methanol APR reaction.[30] Furthermore, hydrophilic surfaces facilitate the rapid removal of gas bubbles, aiding hydrogen evolution and preventing the blockage of active sites.[31,32] However, the effect of hydrophilicity of carbon-supported catalysts on gas–solid heterogeneous reactions, such as the WGS reaction, MSR reaction, *etc.*, remains unclear. The WGS reaction operates through two main mechanisms, the redox mechanism proposed by Temkin and the associative mechanism.[33–35] Keiski *et al.* suggested that the redox mechanism is more plausible, with water molecules needing to adsorb on vacant active sites to proceed.[30] Burch *et al.* pointed out that catalyst surface properties are reaction-condition dependent, and higher water concentrations increase the density of OH groups, favoring the redox mechanism.[36] Regardless of the mechanism, the dissociation of H_2O is a rate-limiting step. Investigations into water dissociation during WGS reveal how alkali promoters enhance dissociation at metal-oxide interfaces, and how metal alloys contribute to this process. Optimizing water adsorption and dissociation on catalysts significantly enhances the WGS reaction efficiency.[37,38] While earlier research confirms that hydrophilic catalysts can facilitate WGS and improve hydrogen production, the exact mechanism remains unclear. Specifically, the impact of hydrophilicity on WGS performance and by-product suppression requires further exploration to better understand its role in catalytic behavior and long-term performance.

In this study, we explored how the hydrophilicity/hydrophobicity of carbon-supported Pt-based catalysts affects the WGS reaction. By employing various synthesis techniques, we precisely controlled the hydrophilicity of the carbon support, creating catalysts with varying surface properties. Using these catalysts, a power-law kinetic model was developed to describe the WGS reaction kinetics for PtMnK/AC-Ox catalysts in the temperature range of 150–250 °C. We calculated important parameters such as activation energy, providing a detailed profile of the reaction's kinetic behavior. To further investigate and confirm the impact of catalyst hydrophilicity on activation energy, water molecule adsorption, dissociation rates, and reforming performance, MSR reaction experiments were performed. This study sheds light on the crucial role of hydrophilicity in optimizing water-related reaction performance, offering valuable insights for future catalyst design and understanding of catalyst structure–reactivity relationship.

2. Methods

2.1. Synthesis of catalysts

The catalysts were prepared with minor modifications based on our previous research.[28] Initially, activated carbon (AC) was crushed and placed in a round-bottom flask containing 200 mL of a 20 wt% $KMnO_4$ solution. The mixture was stirred and heated to 343 K and maintained under reflux for 3 h. The AC was then thoroughly rinsed, and the resulting slurry was dried at 333 K in an oven overnight. A 2 wt% PtMnK/AC-Ox catalyst was prepared by impregnation of an

aqueous solution of the $H_2PtCl_6{\cdot}6H_2O$ precursor, and then the solution was slowly added to $KMnO_4$-treated AC, continuously stirred, and kept at room temperature for 12 h. The resulting mixture was then heated to 323 K and stirred until a paste was formed, which was subsequently dried at 333 K overnight.

A 2 wt% PtMnK/AC catalyst was prepared by a sequential impregnation method. $Mn(NO_3)_2{\cdot}6H_2O$ (manganese nitrate hexahydrate) and KNO_3 (potassium nitrate) solution was slowly added to AC, continuously stirred, and kept at room temperature for 12 h. The mixture was then heated to 323 K and stirred until it formed a paste, and dried at 333 K in an oven overnight. And then the impregnation of aqueous solution of $H_2PtCl_6{\cdot}6H_2O$ is performed, which is the same as the above process.

After the impregnation step, the catalysts were calcined *in situ* under N_2 with a flow rate of 50 mL min^{-1} at 623 K for 2 h and then reduced by H_2 with a flow rate of 30 mL min^{-1} at 523 K for 2 h prior to the reactions. The metal contents of Pt, Mn and K of PtMnK/AC by a sequential impregnation method are close to those of PtMnK/AC-Ox prepared by impregnation of Pt on $KMnO_4$-modified AC.

2.2. Characterization of catalysts

The contact angle of the catalyst was characterized by the sessile drop method (Kino SL 250, USA). The contact angle was determined by drawing a tangent close to the edge of the droplet. And its value was determined by averaging three measurements taken at different locations on the catalyst surface. The textural properties of the catalysts were analyzed based on N_2 adsorption desorption isotherms measured at −196.15 °C using a specific surface area and micropore analyzer (Micromeritics, BSD-PM2, BSD Instrument). CO temperature-programmed desorption (CO-TPD) was performed using an AutoChem 2920 instrument. 100 mg of the sample was initially heated in air at 300 °C for 1 h and then cooled to room temperature. CO gas (20 mL min^{-1}) was introduced into the sample chamber for five minutes. After complete CO adsorption, He gas (40 mL min^{-1}) was introduced to purge the chamber for 0.5 h to remove excess CO gas. The sample chamber temperature was then increased at a rate of 10 °C min^{-1}, and the resulting signal was recorded using a mass spectrometer detector. Electron paramagnetic resonance (EPR) was performed on a Bruker EMXplus-10/12 spectrometer.

2.3. Catalytic performance tests

2.3.1. Water–gas shift reaction. The reaction device consists of two main sections, the heating section and the reaction section, as shown in Fig. 1. The heating section employs computerized temperature-controlled electric heating, allowing precise control of the heating rate and precise maintenance of the reaction temperature. The test device comprises a tube furnace with a quartz tube (400 mm long, 14 mm inner diameter). The upper end of the quartz tube serves as the inlet, while the lower end is the outlet, both connected with flanges. A nitrogen stream is introduced at the inlet, while the outlet is connected to the mixed raw gas (CO and N_2). A microinjector pump at the inlet slowly injects distilled water into a high-temperature preheater to generate steam. The resulting steam mixes with the raw gas and enters the reaction device simultaneously. The outlet collects condensed steam from the reaction and is equipped with a flow meter to measure the gas flow. The flow meter determines the gas flow rate, and the gas composition is analyzed in real time using gas chromatography.

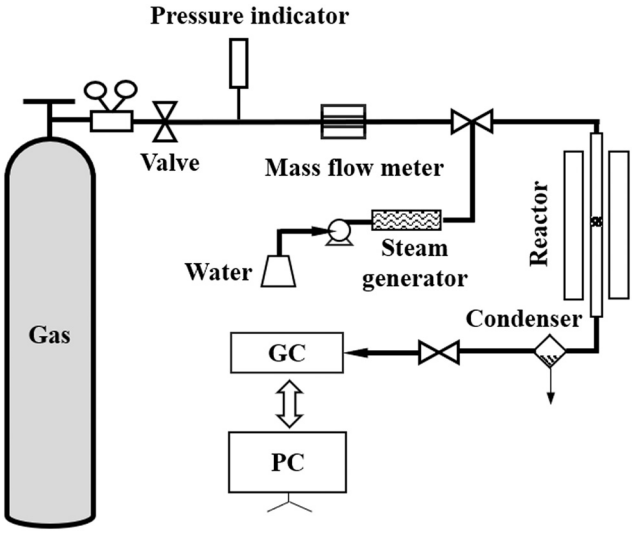

Fig. 1 Schematic illustration of the fixed-bed experimental setup.

The experimental procedure involved the use of 0.2 g of catalyst for the kinetic experiments. To ensure the stability of the experimental process and the accuracy of the data, air tightness is verified. This is done by opening the nitrogen valve, adjusting the pressure in the reaction system to 0.5 MPa, and maintaining this nitrogen pressure for 10 minutes, ensuring the required conditions are met.

To ensure the reliability of the results obtained under the aforementioned test conditions, it is essential to eliminate potential internal variables aside from the setup and operational factors. Preliminary tests are necessary to confirm the absence of any confounding factors. The objective of the blank experiment is to determine if the materials used in the fixed bed impact the reaction process. Since the WGS reaction is a heterogeneous reaction, it is important to examine the effect without the addition of a catalyst.

The objective of the stability experiments is to assess how the reaction process remains consistent over time. The reaction process is divided into three stages, an initial stage, a stabilization stage, and a finish stage. Preliminary experiments are necessary to determine the time required for the process to reach the stabilization stage.

For the diffusion experiment, both internal and external diffusion influences on the WGS reaction are examined. The

impact of internal diffusion is assessed by analyzing the correlation between the particle size of the catalyst and the reaction. The effect of external diffusion is evaluated by examining the relationship between the mass flow rate and the reaction performances.

2.3.2. Methanol steam reforming reaction. The experimental setup for methanol steam reforming comprised a tube furnace with a quartz tube. Initially, a 1 cm layer of quartz wool is placed in the central heated portion of the quartz tube. Another 1 cm layer of quartz wool is placed above the 0.2 g catalyst. The quartz tube is sealed within the furnace, and 70 mL min^{-1} of pure nitrogen is introduced. After reaching the reaction temperature, a 2:1 water-to-methanol molar ratio solution is injected using a syringe pump. The methanol steam reforming reaction is conducted with a gas hourly space velocity (GHSV) of 19 273 mL h^{-1} g_{cat}^{-1}. The liquid substrate is evaporated within the quartz tube and then passes through the catalyst bed. The gaseous product is then collected using a condenser, and its flow rate is measured using a soap bubble flow meter. The gaseous product composition is analyzed using gas chromatography (GC-2014C, Shimadzu, Japan) equipped with a thermal conductivity detector (TCD). The methanol conversion (X_{MeOH}) and hydrogen yield (V_{H_2}) are calculated using the following equations:

$$X_{MeOH} = \frac{F(Y_{CO} + Y_{CO_2} + Y_{CH_4})}{22.4 \times V_{MeOH,in}} \times 100\%$$

$$V_{H_2} = FY_{H_2}$$

where F (m s^{-1}) represents the flow rate of the outlet gas, Y denotes the volume fraction of each gas, and V_{MeOH} (mol s^{-1}) signifies the molar flow rate of methanol injected into the quartz tube *via* the syringe pump.

The reaction conditions for the kinetic experiments are listed in Table 1 below.

2.4. Kinetic modeling and calculations

The equation of the WGS reaction is as follows:

$$CO + H_2O = CO_2 + H_2 \quad (1)$$

The power function macroscopic kinetic model, an empirical model, quickly and efficiently establishes the relationship between the reaction rate and factors such as temperature, pressure, and gas composition.[39,40] In this study, the power function dynamics model was selected for its applicability to industrial production processes. The generalized reaction rate power function model equation for this reaction is as follows:

$$r = Ae^{-E_a/RT}P_{CO}^{l}P_{H_2O}^{m}P_{CO_2}^{n}P_{H_2}^{q}(1-\beta) \quad (2)$$

where A is the pre-exponential; R is the gas constant (8.314 J mol^{-1} K^{-1}); E_a (kJ mol^{-1}) is the activation energy; T is the reaction temperature; P_{CO}, P_{H_2O}, P_{CO_2} and P_{H_2} are the partial pressures of CO, H_2O, CO_2 and H_2, respectively; l, m, n and q represent the number of reaction orders for CO, H_2O, CO_2 and H_2 components; $\beta = \frac{1}{K_{ps}}\frac{Y_{CO_2}Y_{H_2}}{Y_{CO}Y_{H_2O}}$ is the approach to equilibrium.

The impact of the initial partial pressures of H_2O and H_2 on the reaction rate (k) is examined. The experimental results are obtained by varying the initial partial pressure of P_{H_2O} under conditions where the initial partial pressures of P_{H_2} and P_{H_2O} are 0 and P_{CO} is fixed. The results in Table 2 indicate that varying the initial P_{H_2O} does not significantly affect the conversion rate. These findings suggest that the initial P_{H_2O} has no impact on the conversion rate. Similarly, the initial P_{H_2} is found to have no influence on the conversion rate.

It can be demonstrated that the rate of the WGS reaction (k) is a function of the partial pressures of P_{CO_2} and P_{CO} under identical temperature conditions. The reaction rate equation can be shown as follows:

$$-\frac{dP_{co}}{d\tau} = kP_{CO}^{l}P_{CO_2}^{n} \quad (3)$$

In eqn (3), the variable τ (s) is defined as the contact time; it is the ratio of the volume of the catalyst layer to the flow velocity. The conversion rate of CO can be expressed as follows:

$$x = \frac{(P_{co,0} - P_{CO})}{P_{CO,0}} \quad (4)$$

and thus eqn (3) can be rewritten as:

$$\frac{dx}{d\tau} = k(P_{CO,0})^{l+n-1}(1-l)\left(\frac{P_{CO_2,0}}{P_{CO,0}} + x\right)^{n} \quad (5)$$

The proposed levels assume a power of 1 for CO partial pressure and −1 for CO_2 partial pressure. Thus, the rate

Table 1 Summary of experimental conditions for PtMnK/AC-Ox and PtMnK/AC catalysts

Catalyst	Test no.	Temperature (°C)	Contact time[a] (s)	CO volume fraction
PtMnK/AC-Ox	1	150	2.30	0.098
	2	200	0.61	0.098
	3	250	0.38	0.098
PtMnK/AC	4	150	1.52	0.098
	5	200	0.87	0.098
	6	250	0.65	0.098

[a] Contact time values are averaged from repeated experiments under identical conditions.

Table 2 Conversion rates at different temperatures under different initial partial pressures of water

	X_{V1}	X_{V2}	X_{V3}	X_{V4}
150 °C	22.38	21.96	22.12	23.02
250 °C	45.87	44.69	45.21	44.98

equation for the WGS reaction over the PtMnK/AC-Ox catalyst is as follows:

$$-\frac{dP_{CO}}{d\tau} = k\frac{P_{CO}}{P_{CO_2}} \quad (6)$$

and integrating eqn (6) yields the following results:

$$k = -P_{CO,0}\left[x + \left(\frac{P_{CO_2,0}}{P_{CO,0}} + 1\right)\ln(1-x)\right]/\tau \quad (7)$$

As illustrated in eqn (7), when the conversion rate x approaches infinity, the reaction rate k also tends to infinity. Consequently, an amendment to eqn (7) is also necessary:

$$-\frac{dP_{CO}}{d\tau} = k'\frac{P_{CO}}{1 + aP_{CO_2}} \quad (8)$$

In this case, a represents a constant. When the initial partial pressure of CO_2 is set to zero, the integration of eqn (8) is performed as follows:

$$k' = -aP_{CO,0}\left[x + \left(1 + \frac{1}{aP_{CO,0}}\right)\ln(1-x)\right]/\tau \quad (9)$$

When the reaction is close to equilibrium and the reverse reaction cannot be neglected, the rate equation can be approximated as follows:

$$-\frac{dP_{CO}}{d\tau} = k''\frac{P_{CO} - P_{CO,0}}{1 + aP_{CO_2}} \quad (10)$$

where $P_{CO,0}$ is the equilibrium partial pressure of CO. The integration of eqn (10) is performed as follows:

$$k'' = -P_{CO,0}\left[x + \left(x_0 + \frac{1}{aP_{CO,0}}\right)\ln\left(1 - \frac{x}{x_0}\right)\right]/\tau \quad (11)$$

where x_0 is the equilibrium conversion rate of CO.

3. Results and discussion

3.1. Catalyst characterization

Fig. 2 presents the results of simple hydrophilicity tests comparing PtMnK/AC and PtMnK/AC-Ox catalysts as well as the results of their Young's contact angles. In the experiment, 15 mL of deionized water was added to a glass vial, followed by the addition of 0.2 g catalyst. The PtMnK/AC catalyst initially floated on the water surface, with some particles gradually sinking over time. In contrast, the PtMnK/AC-Ox catalyst immediately dispersed into water, forming a uniform suspension. After 15 minutes, the PtMnK/AC catalyst showed clear stratification, with most particles settling at the bottom and a few remaining on the surface. However, the PtMnK/AC-Ox catalyst maintained a turbid and uniform suspension, demonstrating better hydrophilic properties. Fig. 2 further illustrates the comparison of Young's contact angles between the two catalysts. Young's equation describes the relationship between the contact angle and surface tension at the solid–liquid interface.[41] Both catalysts exhibit hydrophilic behavior, as their contact angles are less than 90°. However, the PtMnK/AC-Ox catalyst displays a significantly smaller contact

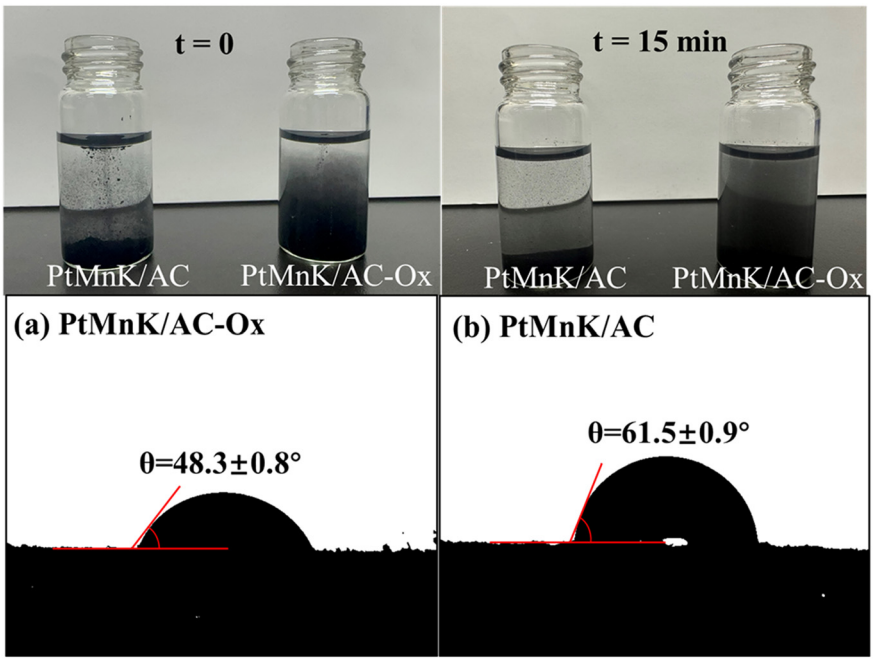

Fig. 2 Hydrophilicity test and contact angle comparison of PtMnK/AC-Ox and PtMnK/AC catalysts.

angle compared to the PtMnK/AC catalyst, confirming its enhanced hydrophilicity. This is attributed to the strong oxidizing properties of $KMnO_4$, which undergoes a redox reaction with the activated carbon during the pretreatment process. This reaction not only results in the deposition of manganese oxides on the surface of the activated carbon but also introduces oxygen-containing functional groups. Similar to acid-washed activated carbon, the presence of these oxygen-containing groups enhances the adsorption capacity for polar molecules. As a result, catalysts pretreated with $KMnO_4$ exhibit improved hydrophilicity.[28]

Fig. 3a displays the N_2 adsorption–desorption isotherms of the catalysts measured at 77 K. The adsorption and desorption isotherms of both catalysts exhibit a distinct hysteresis loop, characteristic of type IV isotherms, which are typically associated with mesoporous materials. This indicates that the materials are predominantly mesoporous (pore size 2–50 nm) and exhibit capillary condensation. The hysteresis loop is of type H3, suggesting the presence of slit-shaped mesopores. Both catalysts show a sharp increase in adsorption at high relative pressures, indicative of macropores (>50 nm) or aggregated pore structures that facilitate the loading of Pt onto the carbon support. Fig. 3b shows the pore size distribution obtained based on the N_2 adsorption and desorption isotherms at 77 K using the non-local density function theory (NLDFT) model. Furthermore, analysis of the data in Table 3 reveals that the pore size distribution of PtMnK/AC-Ox is more concentrated, primarily within the 2–5 nm range, whereas PtMnK/AC exhibits a broader distribution with a higher proportion of macropores.

Previous studies revealed that CO adsorption and desorption are important for regulating gas product distribution in MSR and WGS reactions. The addition of Mn metal as an additive on the catalyst surface was found to limit CO adsorption.[42] The PtMnK/AC-Ox and PtMnK/AC catalysts were prepared using identical proportions of Mn and K. For PtMnK/AC-Ox, $KMnO_4$ was employed as the precursor to introduce both elements. In contrast, PtMnK/AC was synthesized by impregnating the support with $Mn(NO_3)_2{\cdot}6H_2O$ and KNO_3, following a procedure analogous to that used for PtMnK/AC-Ox. Fig. 4a illustrates the CO adsorption and desorption capacities of these catalysts. Desorption peaks observed between 150 °C and 300 °C correspond to the physical adsorption of CO on the pore structure of the carbon support. For the PtMnK/AC catalyst, prepared by impregnation of manganese nitrate and potassium nitrate, the CO desorption peak was slightly lower compared to that of the PtMnK/AC-Ox catalyst, which was modified with potassium permanganate, indicating that the hydrophilicity has little impact on the interaction between the catalyst and CO molecules. However, the PtMnK/AC-Ox catalyst demonstrated higher CO adsorption capacity, which directly influenced the rate of the WGS reaction.

Table 3 Texture data of PtMnK/AC-Ox and PtMnK/AC catalysts

Catalyst	S_{BET} ($m^2\ g^{-1}$)	V_{total} ($cm^3\ g^{-1}$)	Pore size[a] (nm)
PtMnK/AC-Ox	464.7679	0.2663	4.1549
PtMnK/AC	469.5741	0.2551	3.3168

[a] BJH desorption average pore width (4 V $Å^{-1}$).

To determine the effect of the introduction of Mn on the oxygen vacancies of the catalyst, EPR test was performed on the catalyst. As shown in Fig. 4b, the EPR profiles of all catalysts are symmetric about g = 2.002, which is caused by the single-electron O^{2-} radical trapped by the oxygen vacancy.[43] The number of oxygen vacancies is positively correlated with the intensity of the peaks. PtMnK/AC-Ox exhibits a significantly higher number of oxygen vacancies than PtMnK/AC, contributing to its facilitated H_2O adsorption.

3.2. Kinetic modeling and analysis

In the preliminary experiment, the gas components collected without the catalyst showed no notable alteration, indicating that the bed material has no influence on the reaction process. Stability experiments were conducted as well to validate the reliability of the experiment. These experiments demonstrated that after introducing the catalyst and

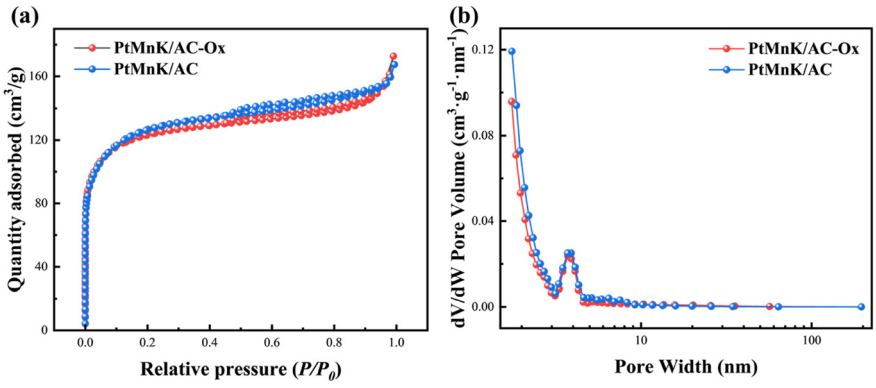

Fig. 3 (a) N_2 adsorption–desorption isotherms for PtMnK/AC-Ox and PtMnK/AC catalysts; (b) pore size distribution of PtMnK/AC-Ox and PtMnK/AC catalysts.

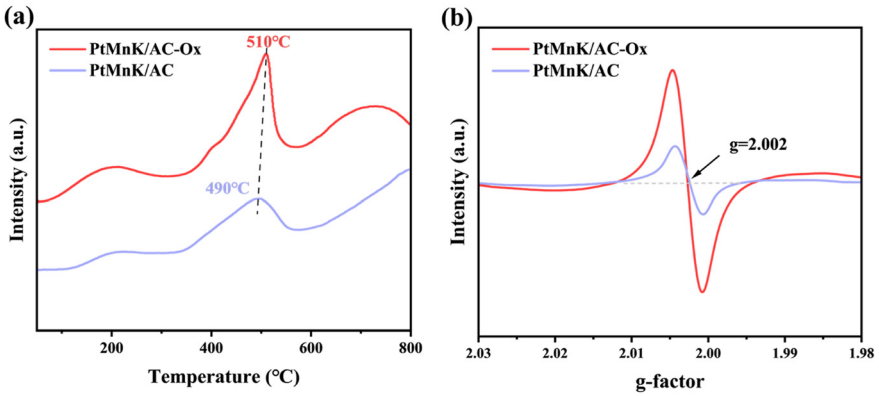

Fig. 4 (a) CO-TPD profiles and (b) EPR profiles of PtMnK/AC-Ox and PtMnK/AC catalysts.

increasing the temperature to initiate the reaction, the gas products were collected and analyzed. As shown in Fig. 5, the CO conversion rate increased rapidly during the first 20 minutes and then stabilized at approximately 12%, indicating that the reaction reached a steady state. The stability of the CO conversion suggests that the catalyst effectively facilitates the reaction and maintains consistent performance over time. This result highlights the reproducibility of the catalytic system under the given experimental conditions and supports its suitability for long-term applications. The short initial stage of this catalytic reaction also contributes to the reliability of kinetic experiments.

To further exclude the effect of internal and external diffusion for improving the accuracy of data, some pre-experiments should be done. Auxiliary experiments revealed that the CO conversion rate decreased progressively as the catalyst particle size exceeded 0.2 mm (Fig. 6a). Consequently, catalysts with particle sizes smaller than 0.2 mm were selected for subsequent experiments. Additionally, it was observed that the CO conversion rate increased as the mass flow rate decreased below 3 L g^{-1} h^{-1}, stabilizing at higher flow rates (Fig. 6b). To eliminate the influence of external diffusion, a mass flow rate greater than 3 L g^{-1} h^{-1} was chosen for the kinetic experiments.

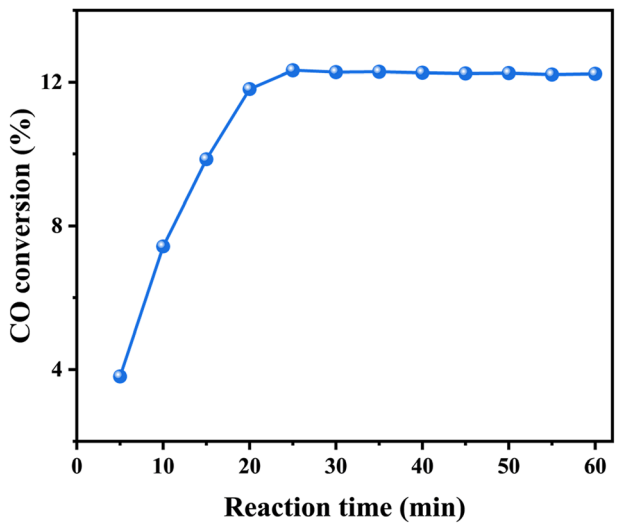

Fig. 5 Stability experiment test of PtMnK/AC-Ox. Reaction conditions: N_2 flow rate: 70 mL min^{-1}, pressure: 0.5 MPa, temperature: 150 °C.

Kinetic experiments were performed at atmospheric pressure over a temperature range of 150 °C to 250 °C, with measurements taken at 50 °C intervals. Four different feed rates were applied at each temperature to vary the contact time and generate a range of CO conversion rates. The results consistently showed a linear relationship between conversion rates and contact time (τ). All WGS experiments maintained a carbon balance error within ±5%, ensuring the reliability of the experimental data. The parameters for the reaction rate equation were determined using a differential method in the non-homogeneous tubular reactor. Using eqn (11), the reaction rate (k'') was calculated. Fig. 6a highlights the sensitivity of CO conversion to catalyst particle size, emphasizing the significance of minimizing internal diffusion effects. Meanwhile, Fig. 6b underscores the importance of achieving sufficient mass flow rates to mitigate external diffusion limitations and maintain stable catalytic performance.

Fig. 7 presents the kinetic experimental data, demonstrating that at a constant temperature, the CO conversion rate decreases as the contact time decreases. Conversely, the CO conversion rate increases significantly with rising temperature, indicating that the reaction is kinetically controlled rather than thermodynamically limited within the reaction temperature range from 150 °C to 250 °C. This behavior aligns with the experimental design, confirming the temperature-dependence of the reaction. Using the kinetic data, the Arrhenius equation was employed to calculate the activation energies (E_{app}) of the WGS reactions over PtMnK/AC-Ox and PtMnK/AC catalysts.

$$\ln k'' = \frac{-E_{app}}{RT} + \ln A \quad (12)$$

As shown in Fig. 8, the linear fit of $\ln k''$ *versus* $1/T$ indicates a strong correlation between the temperature and reaction rate. The apparent activation energy (E_{app}), derived using eqn (12), was determined to be 33.1 kJ mol^{-1} for the PtMnK/AC-Ox catalyst and 54.6 kJ mol^{-1} for the PtMnK/AC catalyst. These

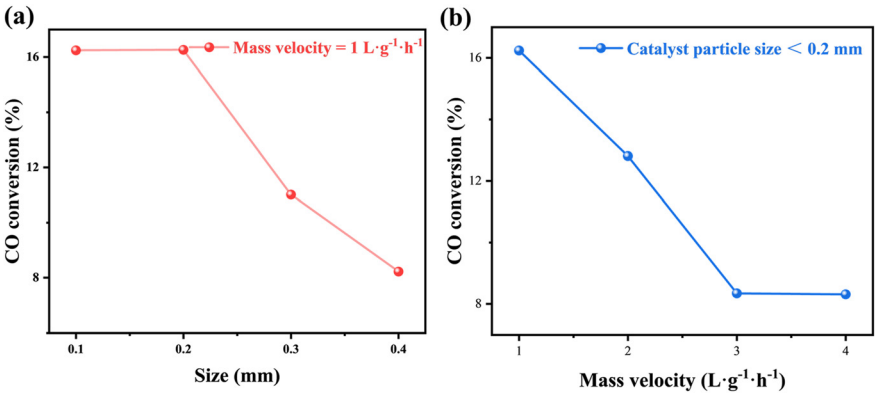

Fig. 6 Results of diffusion experiments on PtMnK/AC-Ox: (a) catalyst particle size and (b) mass flow rate. Reaction conditions: N_2 flow rate: 70 mL min^{-1}, pressure: 0.5 MPa, temperature: 150 °C, reaction time: 60 min.

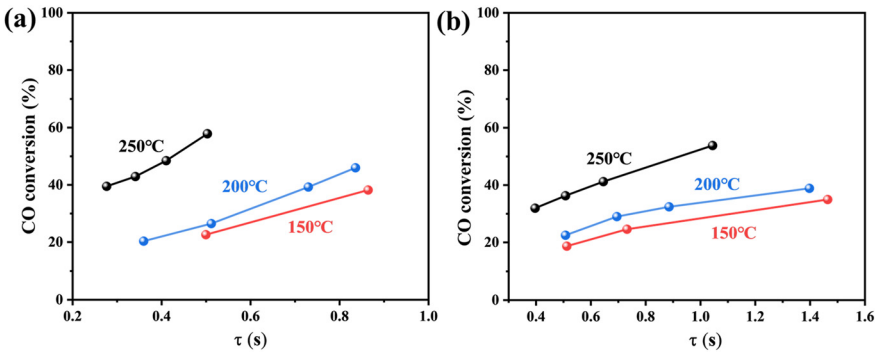

Fig. 7 Kinetic experimental results of (a) PtMnK/AC-Ox and (b) PtMnK/AC catalysts. Reaction conditions: N_2 flow rate: 70 mL min^{-1}, pressure: 0.5 MPa, reaction time: 60 min.

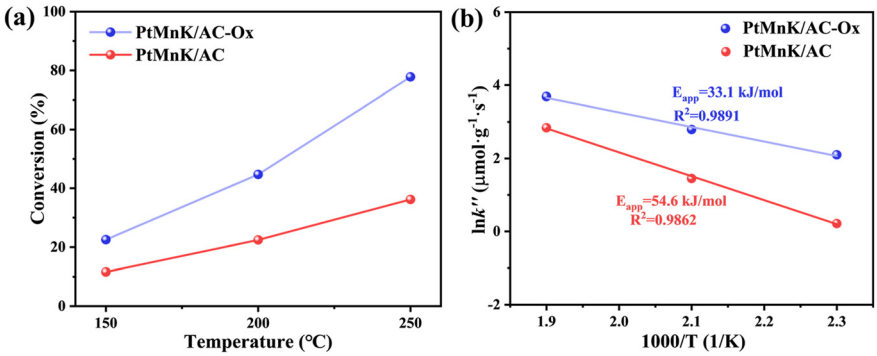

Fig. 8 (a) CO conversion on each catalyst for the WGS reaction at different temperatures and (b) Arrhenius plots of the WGS reaction for PtMnK/AC-Ox and PtMnK/AC catalysts. Reaction conditions: N_2 flow rate: 70 mL min^{-1}, pressure: 0.5 MPa, reaction time: 60 min.

results highlight the higher intrinsic activity of the PtMnK/AC-Ox catalyst, attributing to its enhanced hydrophilicity and efficient water dissociation capabilities. Fig. 9 compares the CO_2/CO ratios of the reaction products at varying contact times and temperatures. At extended contact times, the PtMnK/AC catalyst exhibits a slightly higher CO_2/CO ratio than PtMnK/AC-Ox. However, under normal conditions, the PtMnK/AC-Ox catalyst consistently demonstrates superior WGS activity. This is primarily due to its excellent hydrophilicity, which facilitates the adsorption of H_2O molecules during the first step of the WGS reaction. The dissociation of H_2O on the catalyst surface generates intermediate hydrogen and oxygen species, which subsequently react with the adjacent CO to form CO_2 and H_2, enhancing the overall reaction efficiency. These findings underline the significance of catalyst design, particularly the role of hydrophilicity of carbon-supported catalysts and their activation energy, in optimizing the WGS reaction.[44] The PtMnK/AC-Ox catalyst outperforms PtMnK/AC due to its lower activation energy and superior water

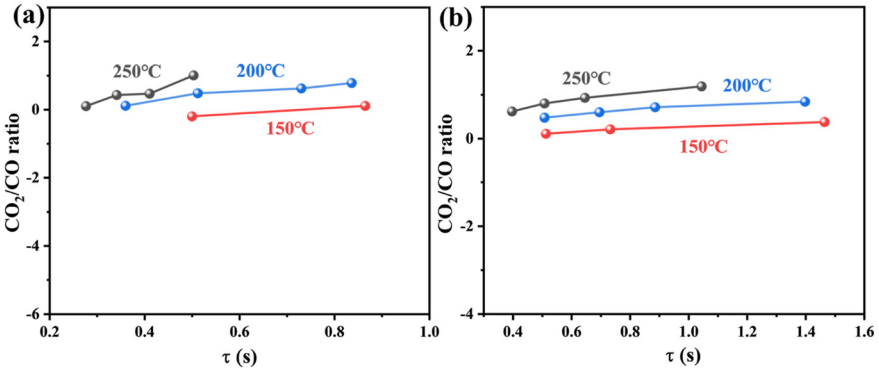

Fig. 9 CO_2/CO ratios at different contact times of (a) PtMnK/AC-Ox and (b) PtMnK/AC catalysts. Reaction conditions: N_2 flow rate: 70 mL min^{-1}, pressure: 0.5 MPa, reaction time: 60 min.

adsorption, making it a promising candidate for hydrogen production applications.

The model was tested and confirmed for better accuracy. As shown in Table 4, the *R*-value close to one indicates higher model precision, while the *F*-value reflects the ratio of the regression mean square to the residual mean square. $F_{0.05}$ denotes the critical *F*-statistic at a 5% confidence level for the given degrees of freedom. A model is deemed reliable if its *F*-value exceeds 10 × $F_{0.05}$. The statistical test results, presented in Table 4, demonstrate that both models for the as-prepared catalysts are highly precise, with *R*-values close to one. Additionally, their *F*-values significantly exceed 10 × $F_{0.05}$, confirming the robustness and reliability of the models.

Subsequently, a comparative analysis was performed to evaluate the activation energy (E_{app} = 33.1 kJ mol^{-1}) of the PtMnK/AC-Ox catalyst in this work against those in previous studies. As shown in Table 5, the PtMnK/AC-Ox catalyst, prepared using the $KMnO_4$-treated carbon support, exhibits a notably lower activation energy compared to other Pt-based catalysts. This lower activation energy highlights the superior performance of the catalyst for the WGS reaction, particularly in promoting efficient CO conversion.

Our previous study have demonstrated that the hydrophilicity of catalysts enhances the aqueous phase reforming of methanol for hydrogen production in an aqueous reaction environment.[28] However, further research is required to investigate the role of catalyst hydrophilicity in the adsorption and dissociation of gaseous H_2O and its effect on the performance of methanol steam reforming. To address this, PtMnK/AC-Ox and PtMnK/AC catalysts have been used in the methanol steam reforming reaction to compare their catalytic performance under controlled conditions. As shown in Fig. 10, the experiments were conducted with 0.2 g of catalyst, a gas hourly space velocity (GHSV) of 19 500 mL h^{-1} g_{cat}^{-1}, and a water-to-methanol molar ratio of 2 : 1. The PtMnK/AC catalyst achieved a methanol conversion rate of 75.4% at 400 °C. In contrast, the PtMnK/AC-Ox catalyst demonstrated significantly improved performance, achieving a methanol conversion of 88.9%. Furthermore, the product selectivity differed markedly over these two catalysts. The PtMnK/AC-Ox catalyst exhibited a lower CO selectivity of 5.1% compared to 13.4% for PtMnK/AC, alongside a higher H_2 yield of 77.0%, compared to 62.3% for PtMnK/AC. This indicates that PtMnK/AC-Ox displays superior catalytic efficiency, particularly in the WGS reaction activity. Kinetic analysis further validated these findings. The methanol steam reforming reaction typically involves two primary steps: the dissociation and dehydrogenation of methanol, followed by the WGS reaction.[13,44] The activation energy for methanol dissociation was significantly higher than that for the WGS reaction. In the WGS reaction, the CO reaction and desorption emerged as a pivotal step. The ability of CO, an intermediate product of methanol dehydrogenation, to effectively react with other intermediates and desorb determines the subsequent reaction pathway, which affects the production distribution remarkably. CO-TPD results in Fig. 4a revealed that the PtMnK/AC-Ox catalyst exhibited a higher CO adsorption/desorption capacity, with a peak at approximately 510 °C, compared to 490 °C for PtMnK/AC. This indicates stronger CO adsorption and higher

Table 4 Statistical test results of kinetic models

Kinetic model	*M*	M_p	*R*	*F*	$F_{0.05}$
PtMnK/AC-Ox	12	2	0.9891	182.7	0.04
PtMnK/AC	12	2	0.9862	252.1	0.06

Table 5 Comparison of activation energies of the WGS reaction over supported catalysts

Serial number	Catalyst	Activation energy (kJ mol^{-1})	Ref.
1	PtMnK/AC-Ox	33.1	This work
2	PtMnK/AC	54.6	This work
3	2%Au/α-MoC	22.0	Ma *et al.*[45]
4	Pt/MoC	38.0	Rodriguez *et al.*[46]
5	Rh/CeO_2	52.0	Somorjai *et al.*[44]
6	Pt@mp-CeO_2	60.0	Tao *et al.*[47]
7	Pt/CeO_2	55.0	Roh *et al.*[48]
8	Pt/MnO_x	78.0	Geng *et al.*[49]

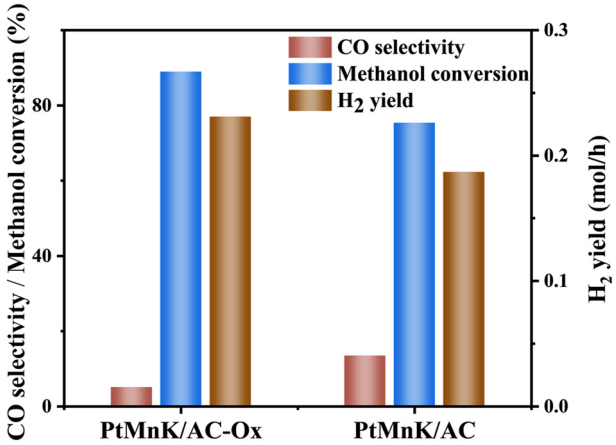

Fig. 10 Hydrogen production efficiency, methanol conversion and product selectivity of PtMnK/AC-Ox and PtMnK/AC catalysts for methanol steam reforming at 400 °C.

adsorption capacity on PtMnK/AC-Ox, attributed to enhanced hydrophilicity and synergistic interactions between Pt and MnO_x on the carbon support. Additionally, the PtMnK/AC-Ox catalyst with higher hydrophilicity displayed a greater capacity for water molecule adsorption and dissociation, which significantly reduced the activation energy for the WGS reaction. It can be concluded that enhanced hydrophilicity facilitated the adsorption of gaseous and liquid H_2O molecules, leading to their dissociation into free oxygen and hydrogen. This enabled efficient CO conversion into CO_2 and H_2. Moreover, the rapid reaction of CO by the WGS reaction on the Pt sites contributed to a higher CO_2 selectivity, as observed in the redox reaction mechanism. In this pathway, CO reacts with dissociated OH groups from H_2O to form formate intermediates, which subsequently decompose into CO_2 and H_2, rather than the methanation reaction due to the strong interaction between Pt and CO.[50–53] These findings demonstrate that improving the hydrophilicity of the catalyst enhances CO desorption and water dissociation capacities, effectively suppressing methanation while promoting hydrogen production by the WGS reaction route. The superior performance of PtMnK/AC-Ox highlights the critical role of catalyst design, especially the hydrophilicity of carbon-supported catalysts in optimizing steam reforming processes for sustainable hydrogen production.

In association with the kinetic studies of the WGS reaction over PtMnK/AC-Ox and PtMnK/AC catalysts, calculations revealed that the activation energy (E_{app}) of PtMnK/AC-Ox is 33.1 kJ mol^{-1}, significantly lower than that of PtMnK/AC (54.6 kJ mol^{-1}). As shown in Fig. 8a, the PtMnK/AC-Ox catalyst exhibited a higher CO conversion rate within the temperature range of 150 °C to 250 °C, highlighting its superior performance. The enhanced hydrophilicity of the carbon support plays a vital role in facilitating efficient interactions between water molecules and the active sites of the catalyst. Compared to PtMnK/AC, PtMnK/AC-Ox contains more oxygen-containing functional groups, which significantly improve its hydrophilicity. Better hydrophilicity enhances its ability to adsorb and dissociate water molecules during the WGS reaction. This improvement also reduces the activation energy of the methanol steam reforming reaction, thereby promoting the efficient conversion of CO intermediates to CO_2 without blocking Pt active sites required for methanol dehydrogenation. For the methanol steam reforming reaction, methanol molecules undergo dehydrogenation at platinum sites, producing CO, which is adsorbed on the catalyst surface. The PtMnK/AC-Ox catalyst efficiently desorbs CO and, due to its enhanced hydrophilicity, adsorbs and dissociates water molecules. Then, the reaction of adsorbed CO and H_2O forms CO_2 and H_2 by redox pathways. These mechanisms are schematically illustrated in Fig. 11. Hydrophilic catalysts demonstrate a strong ability to adsorb and dissociate water molecules in both methanol aqueous phase reforming and methanol steam reforming.

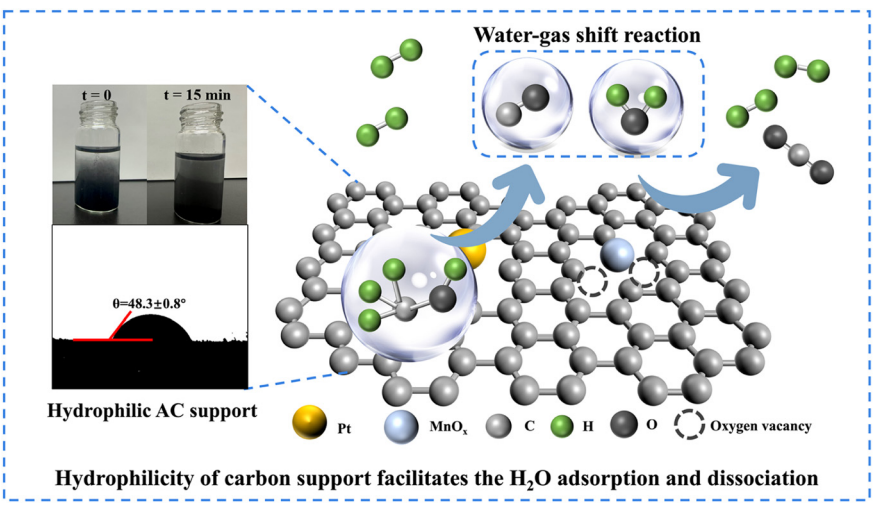

Fig. 11 Schematic illustrations of the mechanism of methanol steam reforming over the PtMnK/AC-Ox catalyst.

For the methanol aqueous phase reforming reaction, a high concentration of water around the catalyst increases the surface OH group concentration, further promoting the dissociation of H_2O into O_{ad} and H_{ad}. This makes the redox mechanism dominant in the WGS reaction.[54] In this study, the methanol steam reforming reaction also involved WGS reactions. Additionally, as illustrated in Fig. 4b, oxygen vacancies on the MnK/AC support promote the WGS reaction through the redox mechanism, as detailed in Fig. 11. The superior hydrophilicity of PtMnK/AC-Ox not only facilitates efficient water dissociation but also suppresses undesired methanation, resulting in higher hydrogen yield and CO_2 selectivity. These characteristics underscore the importance of catalyst hydrophilicity in optimizing the steam reforming process for efficient hydrogen production with less gaseous by-products such as CH_4, CO, *etc.*

4. Conclusions

In this study, two catalysts with different hydrophilicity were used for the kinetic experiments of the WGS reaction. The activation energy of the PtMnK/AC-Ox catalyst was calculated to be E_{app} = 33.1 kJ mol^{-1}, which is lower than that of the PtMnK/AC catalyst with E_{app} = 54.6 kJ mol^{-1}. The $KMnO_4$-treated carbon support is rich in hydrophilic groups, which facilitates the dissociation of H_2O to produce free oxygen and hydrogen, and thus improves the hydrophilicity of the catalyst surface. This improvement facilitates the association with CO intermediates and possible redox reactions, increasing the efficiency of the WGS reaction. With lower activation energy and enhanced H_2O adsorption and dissociation capabilities, the PtMnK/AC-Ox catalyst achieved higher hydrogen yield and CO_2 selectivity in the steam reforming reaction. This variation state induced WGS reaction activity by regulating the adsorption, dissociation, and migration of CO and H_2O molecules. Moreover, the hydrophilic catalysts exhibited their properties in both aqueous phase and steam reforming of methanol, efficiently adsorbing and dissociating liquid or gaseous water molecules, which facilitated the WGS reaction. Based on this study, it provided a theoretical basis and guidance for the rational design of catalysts and the influence of hydrophilicity of carbon-based catalysts on water-related reactions.

Data availability

The authors do not have permission to share data.

Conflicts of interest

The authors declare that they have no known competing financial interests or personal relationships that could have appeared to influence the work reported in this paper.

Acknowledgements

This work was financially supported by the National Key R&D Program of China (2023YFE0206000), the National Natural Science Foundation of China (No. 52476189), the Science and Technology Development Fund, Macao SAR, China [0030/2022/A1] and the Macao Young Scholars Program (AM2023006).

References

1 S. Balibar, *C. R. Phys.*, 2017, **18**, 479–487.
2 P. Nunes, F. Oliveira, S. Hamacher and A. Almansoori, *Int. J. Hydrogen Energy*, 2015, **40**, 16408–16418.
3 M. Niermann, S. Timmerberg, S. Drünert and M. Kaltschmitt, *Renewable Sustainable Energy Rev.*, 2021, **135**, 110171.
4 S. Singh, S. Jain, V. Ps, A. Tiwari, M. Nouni, J. Pandey and S. Goel, *Renewable Sustainable Energy Rev.*, 2015, **51**, 623–633.
5 F. Meng, C. Dai, Z. Liu, S. Luo, J. Ge, Y. Duan, G. Chen, C. Wei, R. Chen, J. Wang, D. Mandler and Z. Xu, *eScience*, 2022, **2**, 87–94.
6 S. Verhelst, J. Turner, L. Sileghem and J. Vancoillie, *Prog. Energy Combust. Sci.*, 2019, **70**, 43–88.
7 Z. P. Tian, Y. H. Lu, J. Y. Wang, R. Y. Shu, C. Wang and Y. Chen, *Fuel*, 2024, **357**, 129691.
8 Z. Y. Zheng, Y. X. Ge, W. W. Lu, Y. Y. Zhou, H. P. Zhu, P. X. Gao, C. M. Li, W. Z. Lei, P. C. Zhao, J. J. Li, M. L. Lu and T. J. Wang, *Fuel*, 2025, **382**, 133775.
9 K. Jiao, J. Xuan, Q. Du, Z. Bao, B. Xie, B. Wang, Y. Zhao, L. Fan, H. Wang, Z. Hou, S. Huo, N. P. Brandon, Y. Yin and M. D. Guiver, *Nature*, 2021, **595**, 361–369.
10 N. Bhuvanendran, S. Ravichandran, S. Lee, F. Sanij, S. Kandasamy, P. Pandey, H. Su and S. Lee, *Coord. Chem. Rev.*, 2024, **521**, 216191.
11 J. Li, H. Zhang, Q. Shi, J. Ying and C. Janiak, *Prog. Mater. Sci.*, 2024, **146**, 101335.
12 D. B. Pal, R. Chand, S. N. Upadhyay and P. K. Mishra, *Renewable Sustainable Energy Rev.*, 2018, **93**, 549–565.
13 B. Hu, R. Shu, Z. Tian, C. Wang, Y. Chen and Y. Xu, *Green Chem.*, 2024, **26**, 5485–5498.
14 L. Lin, W. Zhou, R. Gao, S. Yao, X. Zhang, W. Xu, S. Zheng, Z. Jiang, Q. Yu, Y. W. Li, C. Shi, X. D. Wen and D. Ma, *Nature*, 2017, **544**, 80–83.
15 X. Wei, W. Su, Y. Shi, J. Wang, P. Lv, X. Song, Y. Bai, G. Xu and G. Yu, *Int. J. Hydrogen Energy*, 2024, **58**, 128–136.
16 H. Li, L. Wang and F. Xiao, *Catal. Today*, 2023, **418**, 114051.
17 S. Kumar and R. Sahu, *Int. J. Hydrogen Energy*, 2024, **52**, 1498–1506.
18 M. Shokrollahi Yancheshmeh, O. Alizadeh Sahraei, M. Aissaoui and M. Iliuta, *Appl. Catal., B*, 2020, **265**, 118535.
19 T. Bunluesin, R. J. Gorte and G. W. Graham, *Appl. Catal., B*, 1998, **15**, 107–114.
20 M. Hatanaka, N. Takahashi, T. Tanabe, Y. Nagai, K. Dohmae, Y. Aoki, T. Yoshida and H. Shinjoh, *Appl. Catal., B*, 2010, **99**, 336–342.

21 A. S. Oliveira, T. Cordero-Lanzac, J. A. Baeza, L. Calvo, J. J. Rodriguez and M. A. Gilarranz, *Fuel*, 2021, **305**, 121506.
22 Y. Ke, X. Yu, X. Wang, H. Liu and H. Yuan, *Appl. Surf. Sci.*, 2025, **682**, 161674.
23 A. Kostuch, E. Negro, G. Pagot, S. Zoladek, I. Rutkowska, O. Siamuk, A. Chmielnicka, V. Di Noto and P. Kulesza, *Catal. Today*, 2024, **441**, 114889.
24 L. Linganiso, G. Jacobs, K. Azzam, U. Graham, B. Davis, D. Cronauer, A. J. Kropf and C. Marshall, *Appl. Catal., A*, 2011, **394**, 105–116.
25 M. Pazos Urrea, F. Herold, D. Chen and M. Rønning, *Catal. Today*, 2023, **418**, 114066.
26 Z. Tian, Y. Lu, W. Zhang, R. Shu, X. Luo, Q. Song, L. Lei, C. Wang, Y. Chen and L. Ma, *Renewable Energy*, 2024, **230**, 120807.
27 N. M. Schweitzer, J. A. Schaidle, O. K. Ezekoye, X. Pan, S. Linic and L. T. Thompson, *J. Am. Chem. Soc.*, 2011, **133**, 2378–2381.
28 P. Wang, Y. Huang, R. Shu, J. Wang, J. Liu, C. Wang, Z. Tian and Y. Chen, *Mol. Catal.*, 2024, **559**, 114105.
29 T. Li, J. J. Wang, F. L. Wang, L. S. Zhang, Y. Y. Jiang, H. Arandiyan and H. Li, *ChemCatChem*, 2019, **11**, 1576–1586.
30 R. Keiski, T. Salmi, P. Niemistö, J. Ainassaari and V. Pohjola, *Appl. Catal., A*, 1996, **137**, 349–370.
31 B. K. Kim, M. J. Kim and J. J. Kim, *ACS Appl. Mater. Interfaces*, 2021, **13**, 11940–11947.
32 Q. Hu, Z. Wang, X. Huang, Y. Qin, H. Yang, X. Ren, Q. Zhang, J. Liu, M. Shao and C. He, *Appl. Catal., B*, 2021, **286**, 119920.
33 M. Zhu and I. Wachs, *ACS Catal.*, 2015, **6**, 722–732.
34 Y. M. Liu, J. T. Liu, S. Z. Liu, J. Li, Z. H. Gao, Z. J. Zuo and W. Huang, *J. CO2 Util.*, 2017, **20**, 59–65.
35 A. Mohsenzadeh, T. Richards and K. Bolton, *Surf. Sci.*, 2016, **644**, 53–63.
36 R. Burch, *Phys. Chem. Chem. Phys.*, 2006, **8**, 5483–5500.
37 J. Rodriguez, E. Remesal, P. Ramírez, I. Orozco, Z. Liu, J. Graciani, S. Senanayake and J. Sanz, *ACS Catal.*, 2019, **9**, 10751–10760.
38 S. Roy and A. Tiwari, *J. Phys. Chem. C*, 2021, **125**, 13819–13835.
39 Z. H. Li, K. Zhang, W. H. Wang, J. L. Qu, Y. Tian, B. W. Wang and X. B. Ma, *J. Taiwan Inst. Chem. Eng.*, 2016, **68**, 239–245.
40 K. Antoniak-Jurak, P. Kowalik, E. Franczyk, K. Michalska, R. Bicki and W. Próchniak, *Fuel*, 2024, **357**, 129758.
41 D. M. Liu, C. Dong, J. P. Zhong, S. L. Ren, Y. N. Chen and T. S. Qiu, *Carbohydr. Polym.*, 2020, **245**, 116572.
42 W. Zhang, Z. Tian, J. Huang, J. Wang, X. Luo, C. Wang, R. Shu, J. Liu and Y. Chen, *J. Fuel Chem. Technol.*, 2023, **51**, 1791–1804.
43 D. D. Li, Y. Li, X. H. Liu, Y. Guo, C. W. Pao, E. L. Chen, Y. F. Hu and Y. Q. Wang, *ACS Catal.*, 2019, **9**, 9671–9682.
44 L. N. Chen, Z. Y. Qi, X. X. Peng, J. L. Chen, C. W. Pao, X. B. Zhang, C. C. Dun, M. Young, D. Prendergast, J. J. Urban, J. H. Guo, G. A. Somorjai and J. Su, *J. Am. Chem. Soc.*, 2021, **143**, 12074–12081.
45 S. Yao, X. Zhang, W. Zhou, R. Gao, W. Xu, Y. Ye, L. Lin, X. Wen, P. Liu, B. Chen, E. Crumlin, J. Guo, Z. Zuo, W. Li, J. Xie, L. Lu, C. J. Kiely, L. Gu, C. Shi, J. A. Rodriguez and D. Ma, *Science*, 2017, **357**, 389–393.
46 J. A. Rodriguez, P. J. Ramírez and R. A. Gutierrez, *Catal. Today*, 2017, **289**, 47–52.
47 C. Wen, Y. Zhu, Y. Ye, S. Zhang, F. Cheng, Y. Liu, P. Wang and F. F. Tao, *ACS Nano*, 2012, **6**, 9305–9313.
48 D. W. Jeong, W. J. Jang, J. O. Shim, W. B. Han, H. M. Kim, Y. L. Lee, J. W. Bae and H. S. Roh, *Renewable Energy*, 2015, **79**, 78–84.
49 L. Kuai, S. Liu, S. Cao, Y. Ren, E. Kan, Y. Zhao, N. Yu, F. Li, X. Li, Z. Wu, X. Wang and B. Geng, *Chem. Mater.*, 2018, **30**, 5534–5538.
50 Z. Tian, W. Zhang, T. Liu, J. Liu, C. Wang, L. Lei, M. Liao, C. Wang and Y. Chen, *Int. J. Hydrogen Energy*, 2022, **47**, 41468–41479.
51 I. Coronado, M. Stekrova, L. García Moreno, M. Reinikainen, P. Simell, R. Karinen and J. Lehtonen, *Biomass Bioenergy*, 2017, **106**, 29–37.
52 M. Stekrova, A. Rinta-Paavola and R. Karinen, *Catal. Today*, 2018, **304**, 143–152.
53 A. Soares, G. Perez and F. Passos, *Appl. Catal., B*, 2016, **185**, 77–87.
54 D. Li, Y. Li, X. Liu, Y. Guo, C. Pao, J. Chen, Y. Hu and Y. Wang, *ACS Catal.*, 2019, **9**, 9671–9682.